Efficiencies of cobalt- and copper-based coatings applied by different deposition processes for applications in intermediate-temperature solid

Available online at www.sciencedirect.com

ScienceDirect

journal homepage: www.elsevier.com/locate/he

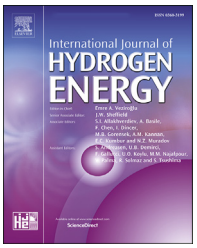

Efficiencies of cobalt- and copper-based coatings applied by different deposition processes for applications in intermediate-temperature solid oxide fuel cells

M. Tomas [a,*], V. Asokan [a], J. Puranen [b], J.-E. Svensson [a], J. Froitzheim [a]

[a] Energy and Materials, Chalmers University of Technology, Kemivägen 10, 41296 Gothenburg, Sweden
[b] Elcogen OY Niittyvillankuja 4, Vantaa 01510, Finland

HIGHLIGHTS

- < 1 μm PVD coatings are as efficient as 10 μm thermal spray coatings at mitigating Cr evaporation.
- PVD Ce/Cu forms a conductive CuO top layer and conductive intermediate spinel.
- PVD Ce/Cu coating are equally good as PVD Ce/Co at 650 °C.

ARTICLE INFO

Article history:
Received 27 April 2022
Received in revised form
12 July 2022
Accepted 19 July 2022
Available online xxx

Keywords:
SOFC
Interconnect
Cu coatings
PVD
Thermal spray
Area specific resistance

ABSTRACT

Solid Oxide Fuel Cells (SOFCs) are electrochemical conversion devices that produce electricity directly by oxidising a fuel. The interconnects between the individual cells need to be coated to limit Cr(VI) evaporation from the steel and to preserve electrical conductivity. Physical Vapour Deposition (PVD)-coated samples with Ce/Co, Ce/Cu, and Ce/MnCu, and Thermal Spray (TS)-coated Mn/Co, Cu and Mn/Cu and AISI 441 steel samples were exposed at 650 °C for up to 1000 h. The PVD Ce/Co and Ce/Cu coatings, as well as the TS Mn/Co coating, exhibited the formation of a thin protective Cr_2O_3 scales underneath the coating. These samples also exhibited the lowest area-specific resistance (ASR) values. The remainder of the samples exhibited much higher mass gains and higher ASR values. Cr(VI) evaporation measurements showed that all the coatings behaved approximately the same despite the PVD coatings being only about one-tenth of the thickness of the TS coatings.

Introduction

As a consequence of increased electricity consumption, power production has become one of the most important issues in Society today [1]. Many systems exist to produce more-sustainable electricity, e.g., solar panels, wind turbines, geothermal, and fuel cells. Fuel Cell (FC) technologies are promising because they exhibit high levels of efficiency, low levels of emissions (NO_x, SO_x, CO_2, etc.), and are versatile.

* *Corresponding author.*
E-mail addresses: tommat@chalmers.se (M. Tomas), jouni.puranen@elcogen.com (J. Puranen).
https://doi.org/10.1016/j.ijhydene.2022.07.168

There most-common types of FCs are Proton-Exchange Membrane Fuel Cells (PEMFCs) and Solid Oxide Fuel Cells (SOFCs) [2]. While PEMFCs use platinum as a catalyst for the reaction to occur at a sufficiently rapid pace, SOFCs operate at high temperatures (≥500 °C) and, thus, do not need expensive catalysts. These systems have different advantages and disadvantages.

On the one hand, PEMFCs have the major drawback that they can only operate with high-purity H_2 as fuel [3]. On the other hand, SOFCs operate at high temperatures, entailing longer start-up times. However, SOFCs are extremely versatile in terms of the fuels that they can use. Given their high electrical efficiency (>60%), low levels of emissions, and fuel flexibility, they represent a promising technology for future energy applications [4–7]. However, poor stability and high cost have limited the commercialisation of SOFCs. One of the key components of an SOFC is the interconnect [8]. Several cells are connected in series to form an FC stack, which forms the core of the FC system. Each cell is electrically connected *via* an interconnect. The interconnects have to fulfil the following requirements: a thermal expansion coefficient (TEC) close to that of the ceramic parts of the cell; low electrical resistance; impermeable to gases; easy to shape; and stability in both high and low pO_2 environments (air on the cathode side and fuel on the anode side) [9,10]. Reduction of the operating temperature of the cell from 1000 °C to 850°C-600 °C, depending on the FC system, allows the use of Ferritic Stainless Steels (FSS) [10]. However, FSS suffer from two major issues under SOFC operating conditions: a) Cr(VI) evaporation from the steel, which poisons the cathode [11]; and b) the growth of a Cr_2O_3 layer, which reduces the electrical conductivity [12]. Nevertheless, steels such as Crofer 22 APU have been used successfully in recent years due to their low production costs, as compared to ceramic interconnects, such as $LaCrO_3$. When exposed to high temperatures and a humid atmosphere, ($CrO_2(OH)_2$) evaporates from the metallic interconnect. To mitigate Cr(VI) vapourisation, the interconnects have to be coated. In the last few years, various coatings have been studied and proposed. Commonly used are manganese (Mn)- and cobalt (Co)-based spinel coatings (Mn/Co), and modified forms of these are considered to be state-of-the-art coatings for this application [13–16]. Instead of applying Mn/Co directly to the steel, a thin metallic layer (600-nm-thick) of Co can be applied [17,18]. This layer will be oxidised to form Co_3O_4 and will be enriched with Mn through diffusion from the steel substrate during stack operation at high temperatures. Another beneficial effect of coatings could be the reduction of the oxide scale growth, as described by *Fontana* et al. [19]. The use of Reactive Elements (RE) has proven to be highly effective at increasing the corrosion resistance of steels [20–23]. The most-common effects of reactive element additions are: increased oxide-scale adhesion and increased resistance to spallation, decreased oxide scale growth, modification of the growth mechanism of the oxide scale, selective oxidation of the alloy. The mechanisms through which REs work are not fully understood. Nevertheless, there is a consensus that the addition of REs changes the Cr_2O_3 scale growth mechanism from pre-dominantly outward growth to pre-dominantly inward growth by oxygen transport. Previous research [24] has shown that the steel strip can be pre-coated with metallic Co and pressed into the desired interconnect shape without increasing Cr(VI) vapourisation. This allows for the mass production of coated interconnects, which reduces the production cost and the eventual price of the interconnects. When oxidised, interconnects form a Cr_2O_3 layer at the metal/oxide interface and a $(Cr, Mn)_3O_4$ spinel top layer that is moderately conductive in the temperature range of the SOFC. As alternatives to Co, different copper-based coatings have been investigated [25–28]. These copper-based coatings behave differently depending on the atmosphere and the deposition process used. In a humid atmosphere, Cu-based coatings decrease corrosion resistance at high temperatures (around and above 800 °C) and result in rapid oxidation. *Petric* et al. [29] have shown that copper spinel oxides are highly conductive, with the highest conductivity being detected for $Cu_{1.3}Mn_{1.7}O_4$ at 225 S cm^{-1} at 750 °C. They concluded that the best candidates for interconnects are ferrite spinels, such as $CuFe_2O_4$, and manganite spinels, such as $Mn_xCo_{3-x}O_4$ or $Cu_xMn_{3-x}O_4$. The utilisation of copper rather than cobalt confers several advantages. For example, the European Union classifies Co as a critical raw material [30]. In addition, cobalt mining is frequently associated with exploitation and child labour [31]. Furthermore, copper is cheaper (10 USD/kg for Cu vs. 70 USD/kg for Co) and less toxic (in dust form) than cobalt (in dust form), and therefore entails a lower risk for health issues [31,32].

The coatings investigated in the present work are coated Ce/Cu, Ce/MnCu, and Ce/Co (as a reference) samples. Additionally, to the different compositions, two different deposition techniques are compared. The above-mentioned coatings are applied employing a PVD process and are compared with a set of similar coatings using a thermal Spray (TS) process: TS Cu, TS Mn/Cu oxide, and TS Mn/Co oxide. The PVD process produces coatings with good adhesion and durability and offers a good control of the thickness and the composition. However, it is commonly considered a high-cost process. Conversely, Thermal Spray process has a reduced cost compared to PVD and faster operating rate. However, the coating microstructure is highly dependent on the operating parameters and the coatings tend to have a higher porosity. The coating thickness ranges from couple of micrometres to few millimetres depending on the process and feedstock.

The aim of this study was to compare the efficiencies of these coatings with respect to the suppression of Cr evaporation and protection against corrosion. Furthermore, two different deposition processes were compared.

Experimental

The characteristics and compositions of the materials used in this study are listed in Tables 1 and 2, respectively.

AISI 441 steel was chosen as the substrate, and the samples were coated on both sides. All the samples produced by Physical Vapour Deposition (PVD) were coated by Sandvik Materials Technology AB. The PVD samples were prepared according to the following procedure: the steel substrate samples were cleaned in a combination of degreasing in ultrasonic bath followed by rinsing in ethanol and de-ionized water before drying in pressurized air. The samples were placed in a

Please cite this article as: Tomas M et al., Efficiencies of cobalt- and copper-based coatings applied by different deposition processes for applications in intermediate-temperature solid oxide fuel cells, International Journal of Hydrogen Energy, https://doi.org/10.1016/j.ijhydene.2022.07.168

Table 1 – Characteristics of the materials used. The coating was applied to the substrate sheets, and the samples were cut out of the steel sheets in the form of 1.5 cm × 1.5 cm coupons.

Material	Deposition process	Coating	
		Inner	Outer
AISI 441	PVD	20 nm Ce	600 nm Cu
AISI 441	PVD	20 nm Ce	600 nm Mn/Cu
AISI 441	PVD	20 nm Ce	600 nm Co
AISI 441	TS	10 μm Cu oxide	
AISI 441	TS	10 μm Mn/Cu oxide	
AISI 441	TS	10 μm Mn/Co oxide	
AISI 441	None	Uncoated	

batch PVD coating chamber and evacuated to 1.10^{-5} mbar while heating the substrate holder to 200 °C before start of the process. The initial step was an exposure to a glow discharge process step for 400 s, to remove adhered species from the substrate surface. The Ce/Cu, and Ce/MnCu coatings, respectively, were deposited using the e-beam evaporation technique from separate crucibles. The coating thickness was measured by using a quartz crystal microbalance (QCM) instrument, calibrated to the processes used. The nominal thickness was 20 nm for the Ce layers and 600 nm for the Cu and MnCu layers, respectively [33]. The TS-generated samples were coated by Kuopion Konepaja Oy [13,15,34,35]. PVD Ce/Co-coated samples with coated edges were also investigated, to compare the Cr evaporation levels with the TS coatings.

Exposures were carried out in horizontal tube furnaces in air that contained 3% water vapour using an air flow of 6000 Sml min^{-1} for up to 1000 h. The mass gain was recorded each week throughout the exposure in a separate experiment, on six different samples. The samples were weighted using a METTLER TOLEDO XP6 scale accurate to the tenth of a microgram.

Cr evaporation

Cr(VI) vapourisation is a significant issue for the longevity of the FC stack. Therefore, it is necessary to quantify the rate of Cr evaporation during the exposure. The Cr vapourisation was measured for all samples using the denuder technique, which allows *in situ* determination of Cr evaporation. A detailed description of the Cr-evaporation measurement procedure can be found elsewhere [36]. Two sets of three samples were exposed in a tubular furnace for 6 weeks, and Cr evaporation measurements were performed each week.

Electron microscopy

Cross-sections of coated AISI 441 samples exposed for 24 h and 1000 h were prepared using the Leica EM TIC 3X Broad Ion Beam (BIB) with an acceleration voltage of 8 kV. The resulting cross-sections were analysed using the JEOL 7800F Prime SEM and FEI Titan 80-300 TEM. SEM Imaging was performed with an acceleration voltage of 10 kV, and Energy Dispersive x-ray (EDX) analysis was carried out with an acceleration voltage of 15 kV. The TEM analysis was performed on a lift-out lamella from the surface realised using the FEI Versa3D Focused Ion Beam (FIB).

Area-specific resistance (ASR) measurement

The samples exposed for 1000 h were mounted in a Probo-Stat™ (NorECs, Norway) measurement cell using a platinum [10] wire and grid to contact the sample electrodes. The resistance was measured by a 2-point, 4-wire method at 650 °C in air, using a current of 100 mA. One point was measured every 2 min for 15 min, at 650 °C, before the cool down of the setup. The ASR was monitored to check for semi-conductive behaviour as the samples cooled down. The ASR measurements were performed on 3 individual samples for each coating. The electrical resistance is characterised by the ASR, which is the measured resistance (R) multiplied by the contact area (A). The measured values are divided by two to account for both surfaces of the sample. A sputter mask of 10 × 10 mm^2 was placed on a pre-oxidised sample, and the sample was then sputtered with gold for 30 min using the Quorum 150 sputter coater and a sputter current of 60 mA. This procedure was then repeated for the reverse side of the sample. The sputtering step was used to produce electrodes with a defined area (1 cm^2) and to ensure adequate contacts between the sample and the platinum electrodes.

Results & discussion

Gravimetric analysis

Fig. 1a shows the average mass gains of the materials exposed at 650 °C in humid air for 1000 h. The uncoated samples exhibited a paralinear behaviour. After 1 week of exposure, the uncoated sample showed a slight increase in mass to $6.9 \cdot 10^{-4}$ mg cm^{-2}, which was followed by a mass loss corresponding to −0.021 mg cm^{-2} after 1000 h of exposure. *Tedmon* et al. [37] have explained this phenomenon in terms of a combination of parabolic growth and mass loss due to vapourisation. In the initial stages of the oxidation process, when the rate of scale growth is significantly higher than the rate of vapourisation, the mass gain follows an approximately parabolic oxidation behaviour. However, once the oxide scale has reached a limiting thickness, the oxide-scale growth rate decreases to become equal to the rate of Cr vapourisation from the oxide scale. At this point, the oxide scale thickness remains constant, and a continuous loss of mass is observed.

Table 2 – Composition of the substrate steel material in weight %, as specified by the manufacturer.

Materials	Fe	Cr	C	Mn	Si	Ni	Ti	Nb	Al	N	P	S
AISI 441 Batch: 89,893	Bal.	17.53	0.016	0.40	0.59	0.15	0.172	0.41	0.007	0.015	0.024	<0.001

Please cite this article as: Tomas M et al., Efficiencies of cobalt- and copper-based coatings applied by different deposition processes for applications in intermediate-temperature solid oxide fuel cells, International Journal of Hydrogen Energy, https://doi.org/10.1016/j.ijhydene.2022.07.168

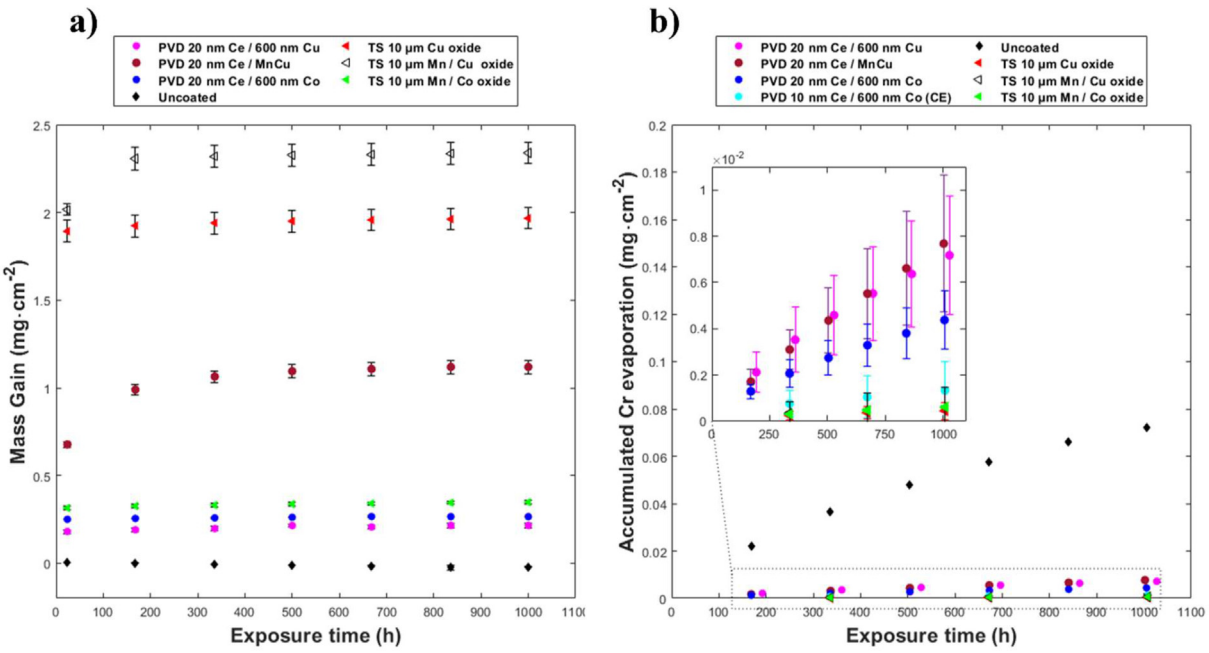

Fig. 1 – a) Average mass gains and b) Cumulative Cr-evaporation level as a function of time for PVD Ce/Cu-coated samples (magenta circles), PVD Ce/MnCu-coated samples (brown circles), PVD Ce/Co-coated samples (blue circles), TS Cu-coated samples (red triangles), TS Mn/Cu-coated samples (empty triangles), and uncoated samples (black diamonds), all of which were exposed for 1000 h at 650 °C in air that contained 3% water vapour. Error bars indicate standard deviation. (For interpretation of the references to color in this figure legend, the reader is referred to the Web version of this article.)

All of the coated samples exhibited rapid mass gains during the first 24 h of exposure, which is, in the case of the PVD Ce/Co- and Ce/Cu-coated samples as well as the TS-MnCo, attributed to the oxidation of the coating. In the other cases, the mass gain is due to a combination of oxidation of the coating and the formation of fast-growing oxides, and the two phenomena cannot be differentiated. The PVD Ce/Cu-coated samples show mass gains that were very similar to those of the PVD Ce/Co-coated samples. After 24 h, the measured mass gain for PVD Ce/Cu-coated samples was 0.18 mg cm^{-2}; this matches well with the theoretical value for converting 600 nm Cu into CuO (~0.13 mg cm^{-2}).

In comparison, the PVD Ce/Co-coated samples displayed a mass gain of 0.25 mg cm^{-2} after 24 h, which also matches well with the theoretical value (~0.19 mg cm^{-2}). After 1000 h of exposure, the mass gain was 0.21 mg cm^{-2} for PVD Ce/Cu and 0.26 mg cm^{-2} for PVD Ce/Co. These results agree very well with the data reported previously by *Falk-Windisch* et al. [38].

The Ce/MnCu-coated samples displayed a rapid mass gain (0.67 mg cm^{-2}) during the first 24 h of exposure, and this continued to increase to 0.99 mg cm^{-2} after 1 week of exposure (168 h), after which it levelled off for the remainder of the exposure period.

The TS Mn/Co coating displayed an initial mass gain of 0.31 mg cm^{-2}. Thereafter, the mass gain of the sample remained almost constant, in similarity to the PVD Ce/Co and Ce/Cu coatings after 1000 h. This indicates that the TS Mn/Co coating is almost fully oxidised at the beginning of the exposure.

This is not the case for either the TS Cu or TS Mn/Cu coatings, which exhibited a strong mass gain in the first 24 h of exposure (~2 mg cm^{-2}), and thereafter a slowing of the rate of mass gain. After the first week, the mass gain was minimal throughout the remainder of the exposure. It seems likely that during deposition not all of the coating was oxidised, such that a part remained in a metallic state. When exposed at high temperature, the metallic part of the coating became oxidised, causing the rapid mass gain observed in the early hours of the exposure. The TS Mn/Cu coating exhibited a slightly higher mass gain than the TS Cu coating.

Cr evaporation measurements

The cumulative Cr-evaporation for uncoated and coated AISI 441 samples exposed for 1000 h at 650 °C is plotted as a function of time in Fig. 1b. Uncoated samples displayed a very high accumulated Cr-vapourisation level of about 0.08 mg cm^{-2} after 1000 h of exposure in humid air. This is in line with previous results from *Falk-Windisch* et al. [39]. In contrast, Ce/Cu-coated samples exhibited a lower Cr-evaporation level, at around $7 \cdot 10^{-3}$ mg cm^{-2} on average, after 1000 h of exposure in 3% water vapour. The Ce/MnCu-coated samples displayed a Cr-vapourisation level of $7.5 \cdot 10^{-3}$ mg cm^{-2} on average after 1000 h of exposure. The Cr(VI) evaporation measured for the Ce/Co-coated samples was $4.4 \cdot 10^{-3}$ mg cm^{-2} on average after 1000 h of exposure. However, this difference should not be over-interpreted, as all the values are very low. A recently published study [40] has

Please cite this article as: Tomas M et al., Efficiencies of cobalt- and copper-based coatings applied by different deposition processes for applications in intermediate-temperature solid oxide fuel cells, International Journal of Hydrogen Energy, https://doi.org/10.1016/j.ijhydene.2022.07.168

shown that samples with coated edges have significantly lower Cr-evaporation levels than the same samples with uncoated edges. To account for this and to compare the PVD coatings (uncoated edges) with the TS coatings with coated edges, a set of Ce/Co-coated samples with coated edges was measured. After 1000 h of exposure, the Ce/Co samples with coated edges exhibited a Cr(VI)-evaporation level of $1.3 \cdot 10^{-3}$ mg cm^{-2} after 1000 h of exposure. Thus the real value for the Ce/Co-coated edges coating is only one-third of the value measured for the uncoated edges, which is in accordance with previous results [40]. The same factor should be applied to the other PVD coatings with uncoated edges. The TS Cu-coated samples displayed a Cr(VI)-evaporation level of $0.3 \cdot 10^{-3}$ mg cm^{-2} after 1000 h of exposure, while the TS Mn/Cu-coated samples exhibited a Cr-vapourisation level of $0.062 \cdot 10^{-3}$ mg cm^{-2} after 1000 h of exposure. Those values are very similar, and both coatings should be considered equivalent in terms of their capacities to mitigate Cr(VI) evaporation. The reference TS Mn/Co-coated samples showed a Cr-vapourisation rate of $0.06 \cdot 10^{-3}$ mg cm^{-2} after 1000 h of exposure, which is similar to the values obtained for the TS Cu- and TS Mn/Cu-coated samples [17,41].

In summary, PVD coatings are as good as TS coatings with respect to mitigating Cr evaporation when the edges are coated, while the coating thickness is thinner by a factor of 10 for the PVD coatings (~1 μm for PVD compared to ~10 μm for TS). This demonstrates the high efficiency of converting a thin metallic coating into a protective oxide at high temperatures.

Microstructural investigation

PVD 20 nm Ce/600 nm Co

A cross-section of the Ce/Co-coated sample is depicted in Fig. 2. Fig. 2a shows the cross-section of the as-received material. The coating thickness is roughly 600 nm. Fig. 2b shows the microstructure of the sample after 24 h of exposure. The top layer is composed of a homogeneous Co_3O_4 spinel, which has a thickness of approximately 1 μm thick, and some pores are evident in this cap layer. A Cr_2O_3 layer is present closest to the metal and is approximately 200 nm in thickness. At the spinel/chromia interface, a thin CeO_2 layer can be observed. After 1000 h of exposure (see Fig. 2c), the sample microstructure is very similar to that at 24 h. The main difference is the diffusion, in the latter, of Mn from the bulk to the cap layer to form a $(Co, Mn)_3O_4$ spinel layer. The chemical analyses at 24 h of exposure and 1000 h of exposure support this observation. Low-level diffusion of Mn (roughly 5 at%) is apparent after 1000 h of exposure.

These results accord with the mass gain measurements. After the first 24 h of exposure, the sample mass gain is slightly increasing during the remainder of the exposure period, which is in agreement with the previous findings of *Falk-Windisch* et al. [38] for samples exposed under the same conditions.

PVD 20 nm Ce/600 nm Cu

The SEM micrographs and the corresponding EDX analysis of a cross-section of an exposed Ce/Cu-coated sample are shown in Fig. 3. Fig. 3a represents the cross-section of the as-received

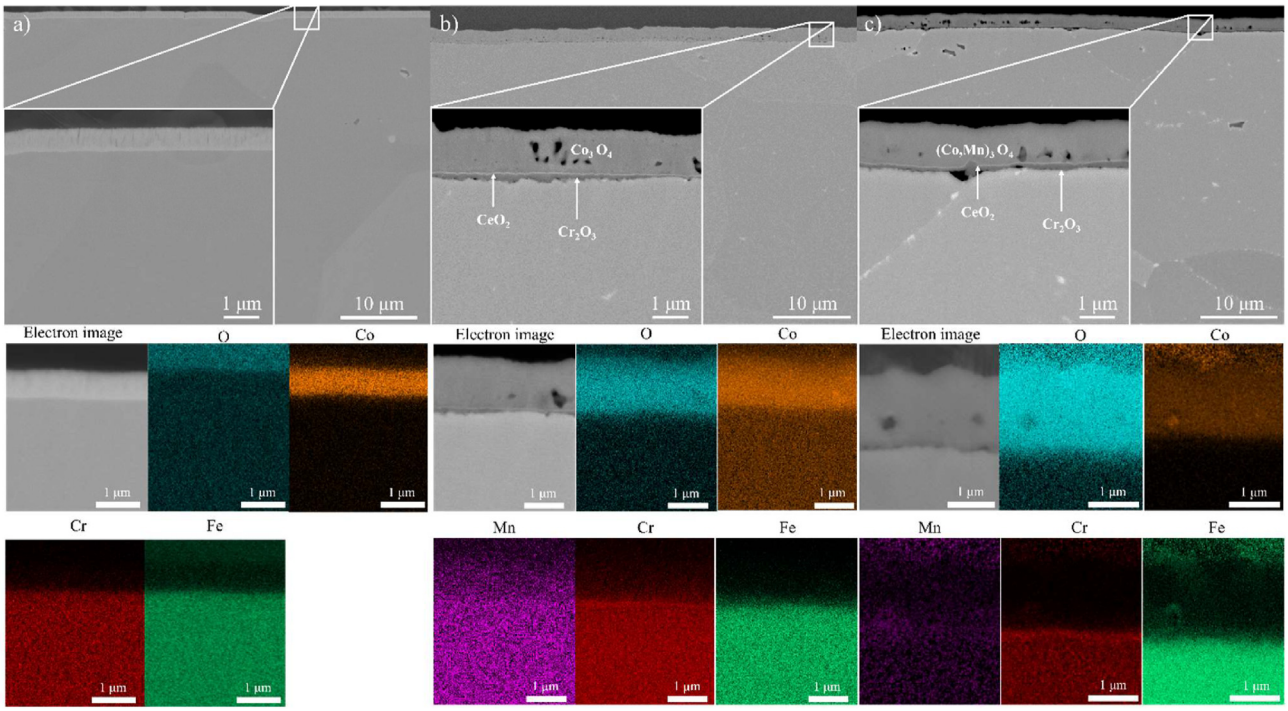

Fig. 2 – a) SEM-Backscattered Electron (BSE) image of a BIB-milled cross-section of the PVD Ce/Co-coated AISI 441 as-received. b) SEM-Backscattered Electron (BSE) image of a BIB-milled cross-section of the PVD Ce/Co-coated AISI 441 exposed for 24 h at 650 °C in air + 3% water vapour. c) SEM-BSE image of a BIB-milled cross-section of the PVD Ce/Co-coated AISI 441 exposed for 1000 h at 650 °C in air + 3% water vapour, together with the corresponding EDS analysis.

Please cite this article as: Tomas M et al., Efficiencies of cobalt- and copper-based coatings applied by different deposition processes for applications in intermediate-temperature solid oxide fuel cells, International Journal of Hydrogen Energy, https://doi.org/10.1016/j.ijhydene.2022.07.168

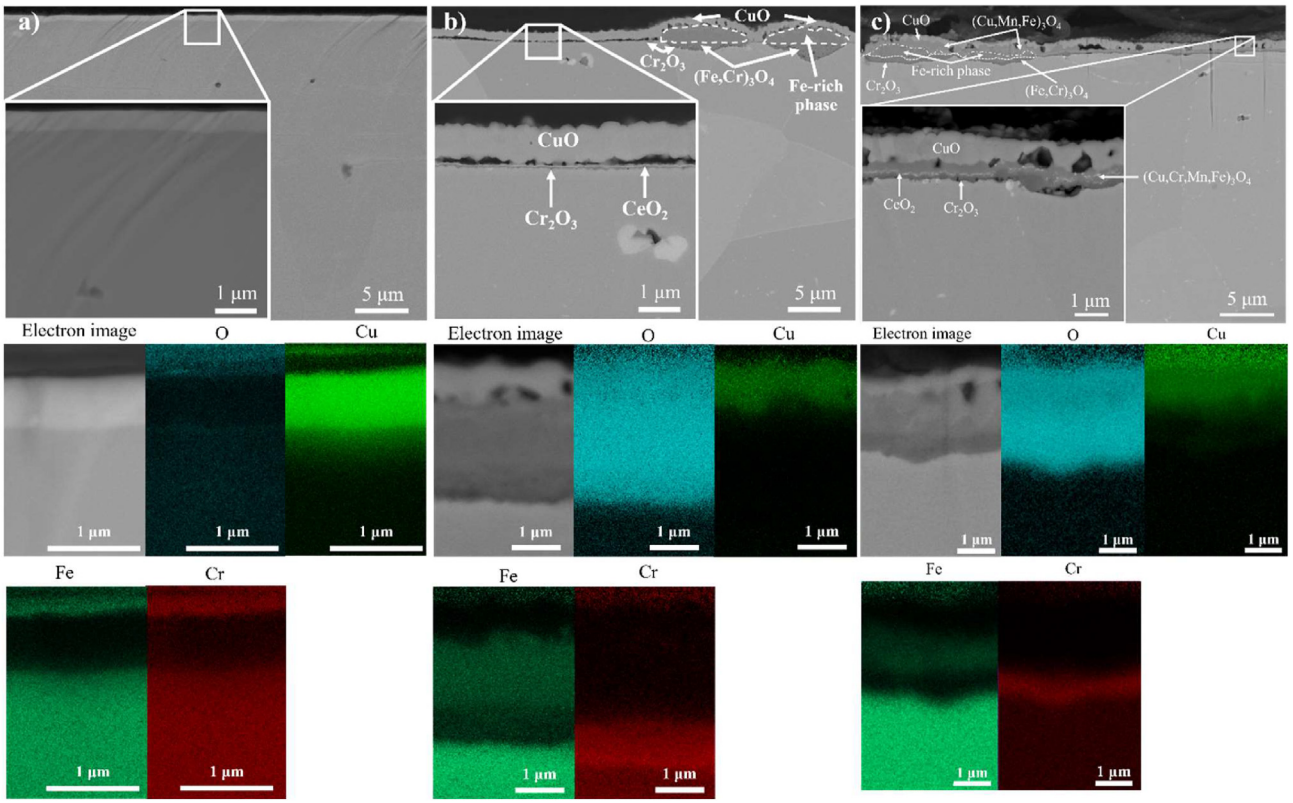

Fig. 3 – a) SEM-Backscattered Electron (BSE) image of a BIB-milled cross-section of the PVD Ce/Cu-coated AISI 441 as-received. b) SEM-Backscattered Electron (BSE) image of a BIB-milled cross-section of the PVD Ce/Cu-coated AISI 441 exposed for 24 h at 650 °C in air + 3% water vapour. c) SEM- BSE image of a BIB-milled cross-section exposed for 1000 h at 650 °C. For a) and b), the corresponding EDS analysis represents the chemical analysis of the nodules.

sample. The coating is roughly 600 nm in thickness. Fig. 3b depicts the sample microstructure after 24 h of exposure. A homogeneous oxide scale mainly covers the surface at an overall thickness of approximately 1 μm. This oxide scale consists of three layers. The top layer has been identified as CuO, the middle layer as a thin spinel oxide, and the third layer as a very thin Cr_2O_3 layer at the metal/oxide interface. Apart from the base oxide, a few oxide nodules (roughly 5 μm in thickness) are spread haphazardly over the surface. These nodules appear to grow an Fe-rich phase under the CuO top layer. Underneath this Fe-rich layer, a $(Fe,Cr)_3O_4$ layer is present, and a Cr_2O_3 layer is found at the metal/oxide interface. The observed nodules with an outer Fe-rich phase and an inward growing $(Fe,Cr)_3O_4$ are a typical morphology observed when the protective oxide scale fails known as breakaway corrosion [42,43]. However, the presence of a Cr-rich layer at the metal oxide interface indicates that the steel contains enough Cr to re-passivate by establishing a protective oxide again. Fig. 3c shows the microstructure of a Ce/Cu-coated sample after 1000 h of exposure. The microstructure is very similar to that seen after 24 h of exposure, indicating a very slow oxidation rate and confirming the presence of a protective Cr_2O_3 layer. The main difference is the presence, in the latter, of an intermediate spinel underneath the CuO cap layer. Overall, the oxide layers formed on the Ce/Cu coating are homogeneous but contain more pores than those formed on the Ce/Co coating [38]. The thermal expansion coefficient for CuO is $11.5 \cdot 10^{-6}$ °C from 300 K to 1073 K [44]. Hence, it is believed that thermal cycling will not affect significantly the CuO cap layer, during operating time.

Within the steel, mainly along the grain boundaries, Nb and Si were observed, indicating the presence of laves phases. The high degree of similarity between the microstructures observed for the 24 h and 1000 h exposures is in line with the observed mass gain curve. The increase in mass within the first 24 h is due to oxidation of the metallic Cu layer and the formation of nodules. The slight increase in sample mass after 24 h of exposure is attributed to the growth of the intermediate layer resulting from the diffusion of Mn, Cr, and Fe and the formation of a Cr_2O_3 layer at the metal/oxide interface.

For a more detailed investigation of the base oxide, EDS analysis on STEM image was performed (Fig. 4). The findings are in line with the SEM observations. There is a relatively pure CuO cap layer of roughly 1 μm in thickness, followed by a thin spinel layer (~300 nm) with high levels of Cu (~40 cation %), Cr (~30 cation%) and Mn (~20 cation%), as well as the presence of Fe in small quantities. *Talic* et al. [45] have suggested that there is faster diffusion of Cr when Cu is present within the spinel. This might explain the high concentration of Cr within the intermediate spinel detected in the TEM

Please cite this article as: Tomas M et al., Efficiencies of cobalt- and copper-based coatings applied by different deposition processes for applications in intermediate-temperature solid oxide fuel cells, International Journal of Hydrogen Energy, https://doi.org/10.1016/j.ijhydene.2022.07.168

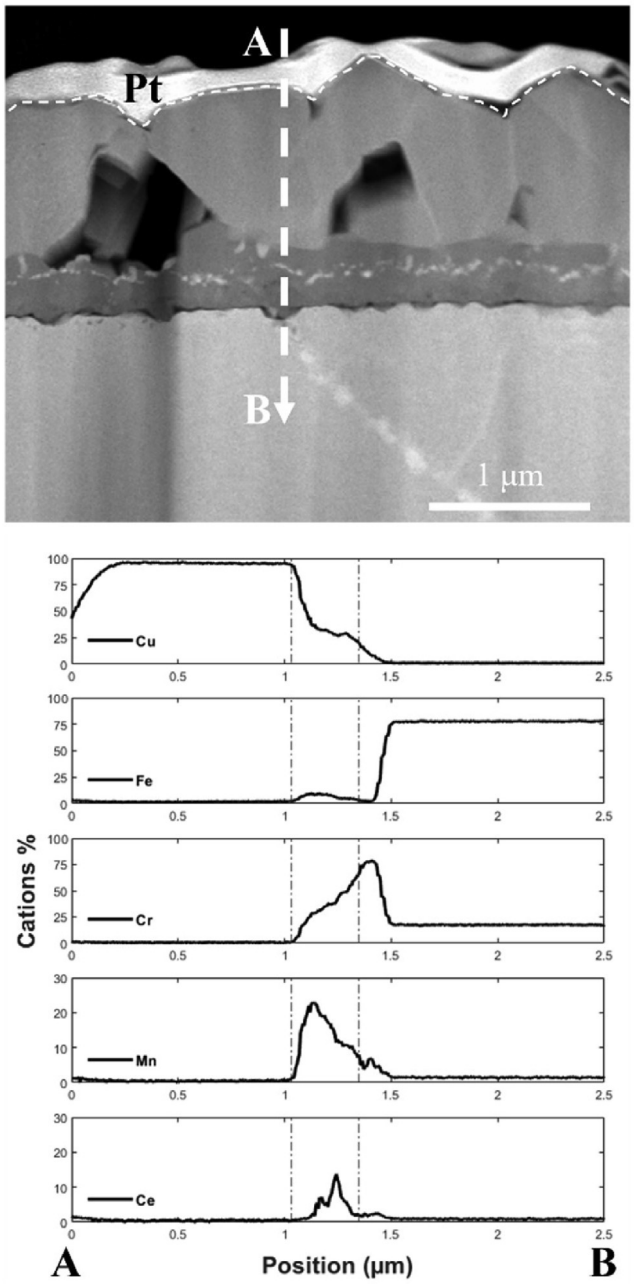

Fig. 4 – STEM analysis of the PVD Ce/Cu-coated AISI 441 exposed for 1000 h at 650 °C in air + 3% water vapour.

elemental analysis. Within the spinel layer, CeO_2 (white line) is evident (see Fig. 4). Closest to the metal, a Cr_2O_3 layer has been formed, which is slightly thicker at the grain boundaries.

PVD 20-nm Ce/MnCu

The microstructural analysis of the Ce/MnCu-coated sample is shown in Fig. 5. Fig. 5a shows the cross-section of the as-received material. The coating is roughly 600 nm in thickness. Fig. 5b represents the sample exposed for 24 h, and Fig. 5c depicts the sample exposed for 1000 h. In both cases, in similarity to the Ce/Cu-coated sample, the oxide scale comprises two microstructures. A thin homogeneous part with a thickness of about 1 μm is interrupted by nodules that are up to 10 μm in thickness. However, in the case of Ce/MnCu, the nodules are more numerous than in the case of Ce/Cu. The mass gain curve indicates some oxide growth after 24 h of exposure (~0.3 mg cm^{-2}), and this correlates with the micrographs that show that the nodules cover most of the sample. Fig. 5b shows that after 24 h of exposure, the homogeneous area displays a top layer composed of an $(Mn,Cu)_3O_4$ spinel layer, and closest to the metal, a Cr_2O_3 layer is identified. The nodule exhibits a top layer composed of Cu and Mn, an Fe-rich oxide middle layer, and a $(Fe,Cr)_3O_4$ layer underneath. An internal oxidation zone is partially encapsulated by a Cr_2O_3 layer (see Fig. 5b).

After 1000 h of exposure, the homogeneous area (see inset in Fig. 5b) shows two different layers. The top layer appears to be a $(Cu,Mn,Fe)_3O_4$ spinel layer. Meanwhile, the oxide layer at the metal/oxide interface was identified as Cr_2O_3. The chemical analysis of the homogeneous layer indicates that the concentration of Cu is higher at the chromia scale interface, whereas the concentration of Mn is higher in the top layer. Fe is also present in the top layer, indicating Fe diffusion from the bulk to the cap layer (not shown). The nodules contain a cap layer that is similar in composition to the homogeneous area. Underneath the $(Cu,Mn,Fe)_3O_4$ cap layer an Fe-rich oxide is found, followed by a spinel layer composed of Cu (~8 at%), Fe (~10 at%) and Cr (~15 at%). Mn seems to only be present at the top of the oxide. Hence, Cu seems to have diffused through the oxide scale throughout the exposure. A chromia layer was identified closest to the substrate, roughly 300 nm in thickness.

A thin ceria layer was observed at the cap layer/chromia interface (insert in Fig. 5b). Laves phases are present inside the bulk, and some Si and Nb are observed along the grain boundaries. The formed layers are continuous and dense, with the consequence that there is a low rate of Cr evaporation throughout the exposure. In summary, the Ce/MnCu performs worse than Ce/Cu, due to the extensive formation of Fe-rich oxide nodules. The reason for this negative effect of Mn is presently unknown.

TS Mn/Co

Fig. 6 depicts the microstructure of the TS Mn/Co-coated sample in the absence of exposure, and after 24 h and 1000 h of exposure, together with the corresponding EDS analysis. Fig. 6a shows a cross-section of the as-received material. The initial thickness is about 10 μm, and the coating has a rough surface. After 24 h of exposure (see Fig. 6b), a homogeneous and thick (~10 μm) $(Mn,Co)_3O_4$ spinel layer can be observed on top, while a very thin Cr_2O_3 layer (of around 200 nm) is visible at the metal/oxide interface. The Mn/Co layer is relatively porous, possibly due to the deposition process [34]. After 1000 h of exposure, the microstructure did not change significantly. The thickness of the top Mn/Co layer remained the same, and the thickness of the chromia beneath was essentially identical in appearance. No other corrosion products were detected. This is in accordance with the mass gain measurements, which were stable throughout the exposure. The lack of a ceria layer does not seem to affect the oxide scale growth, which is still in the same range as those of

Please cite this article as: Tomas M et al., Efficiencies of cobalt- and copper-based coatings applied by different deposition processes for applications in intermediate-temperature solid oxide fuel cells, International Journal of Hydrogen Energy, https://doi.org/10.1016/j.ijhydene.2022.07.168

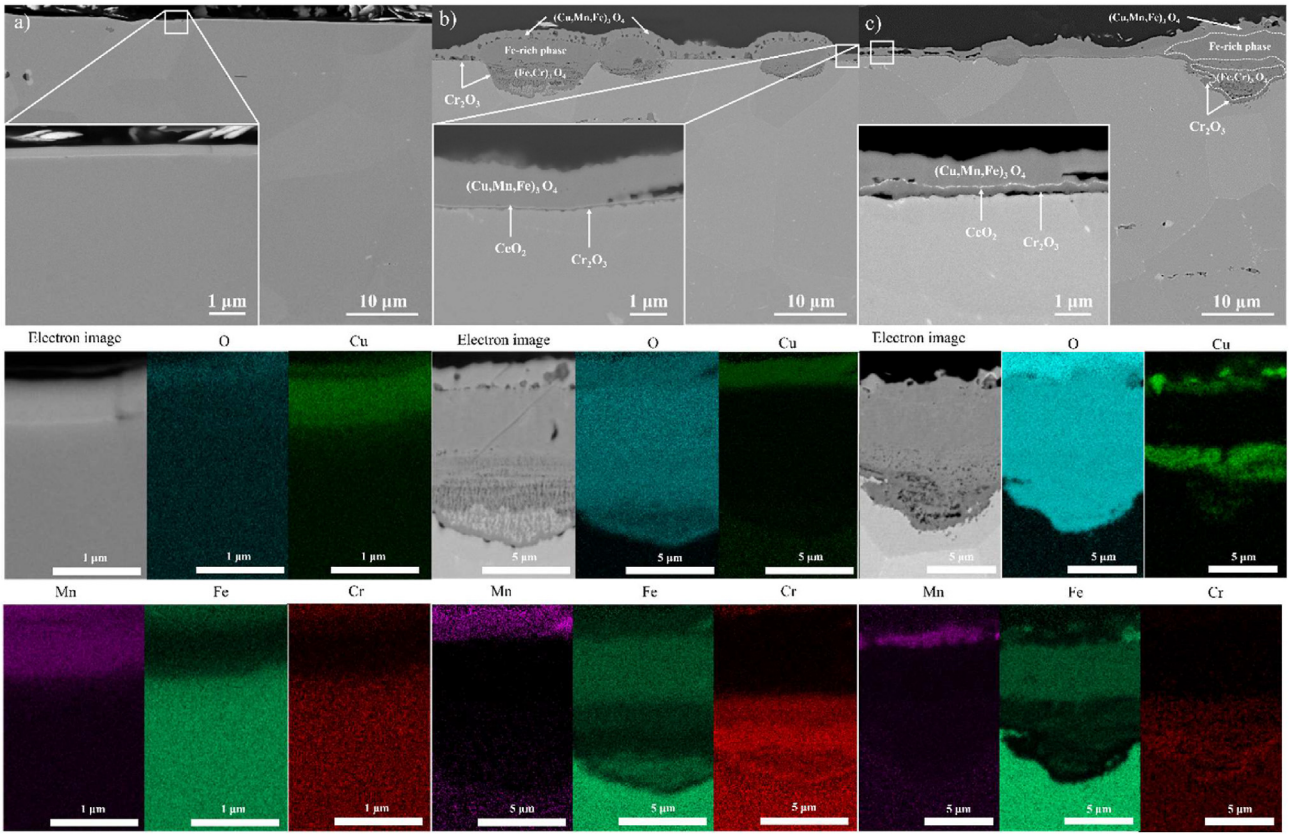

Fig. 5 – a) SEM-Backscattered Electron (BSE) image of a BIB-milled cross-section of the PVD Ce/MnCu-coated AISI 441 as-received. b) SEM-Backscattered Electron (BSE) image of a BIB-milled cross-section of the PVD Ce/MnCu-coated AISI 441 exposed for 24 h at 650 °C in air + 3% water vapour. c) SEM- BSE image of a BIB-milled cross-section of the PVD Ce/MnCu-coated AISI 441 exposed for 1000 h at 650 °C in air + 3% water vapour. The corresponding EDS analysis represents the chemical analysis of the nodules.

the PVD-coated samples, which contain a CeO_2 layer. The very low rate of Cr evaporation can be explained by the relatively thick top Mn/Co layer.

TS Cu

Fig. 7 depicts the microstructural analysis of the TS Cu oxide coating at different exposure times and the corresponding EDS analysis. The as-coated sample (see Fig. 7a) displays a roughly 10-μm-thick coating. EDS analysis showed that part of the coating was still in a metallic state, which is in accordance with the previous assumption regarding the large increase in mass gain at the beginning of the exposure. After 24 h of exposure (see Fig. 7b), the cross-section displayed a top layer of CuO. Beneath it, an Fe-rich oxide layer can be found, followed by an $(Fe,Cr)_3O_4$ spinel layer, and at the metal/oxide interface, a thin Cr_2O_3 layer. The total final thickness is around 20 μm, which is twice as thick as the initial thickness. The CuO top layer is about 10 μm in thickness, which corresponds to the initial thickness of the deposited oxide. The corresponding EDS analysis confirmed the presence of an iron-rich intermediate oxide layer. After 1000 h of exposure (see Fig. 7c), the microstructure did not change, and the oxide layers remained virtually identical. The oxide layers were dense and homogeneous. This is in accordance with the mass gain observation. The high mass gain observed within the first 24 h can be explained by the thick Fe-rich oxide layer formed between the CuO layer and the $(Fe,Cr)_3O_4$ layer. A homogeneous Fe-rich layer is not observed in the case of PVD Ce/Cu-coated sample. This is attributed to the Ce layer which acts as diffusion barrier and impedes Cu from interfering with the formation of a protective Cr_2O_3 scale. A similar mechanism was proposed by *Falk Windisch* et al. [38] in the case of Ce/Co coatings. Furthermore, reactive elements like Ce are known to promote the selective oxidation of Cr_2O_3 [21,46]. The low level of Cr evaporation observed throughout the exposure is due to the thick oxide layers on top of the metal, which constitute a Cr barrier.

TS Mn/Cu

The cross-sections of the TS Mn/Cu-coated sample are depicted in Fig. 8. Fig. 8a exhibits a 10-μm-thick as-received coating. The EDS analysis shows that not all of the coating is oxidised. This might explain in part the high mass gain at the beginning of the exposure. After 24 h of exposure (see Fig. 8b), the micrograph shows six different types of oxides: the top layer is constituted of a CuO oxide layer, while beneath it lie a $(Cu,Mn)_3O_4$ layer and an Mn-rich layer. The presence of these three phases could be linked to the deposition process, i.e., TS powder-precursor. Beneath the top three layers, the cross-section exhibits the corrosion products: an Fe-rich oxide

Please cite this article as: Tomas M et al., Efficiencies of cobalt- and copper-based coatings applied by different deposition processes for applications in intermediate-temperature solid oxide fuel cells, International Journal of Hydrogen Energy, https://doi.org/10.1016/j.ijhydene.2022.07.168

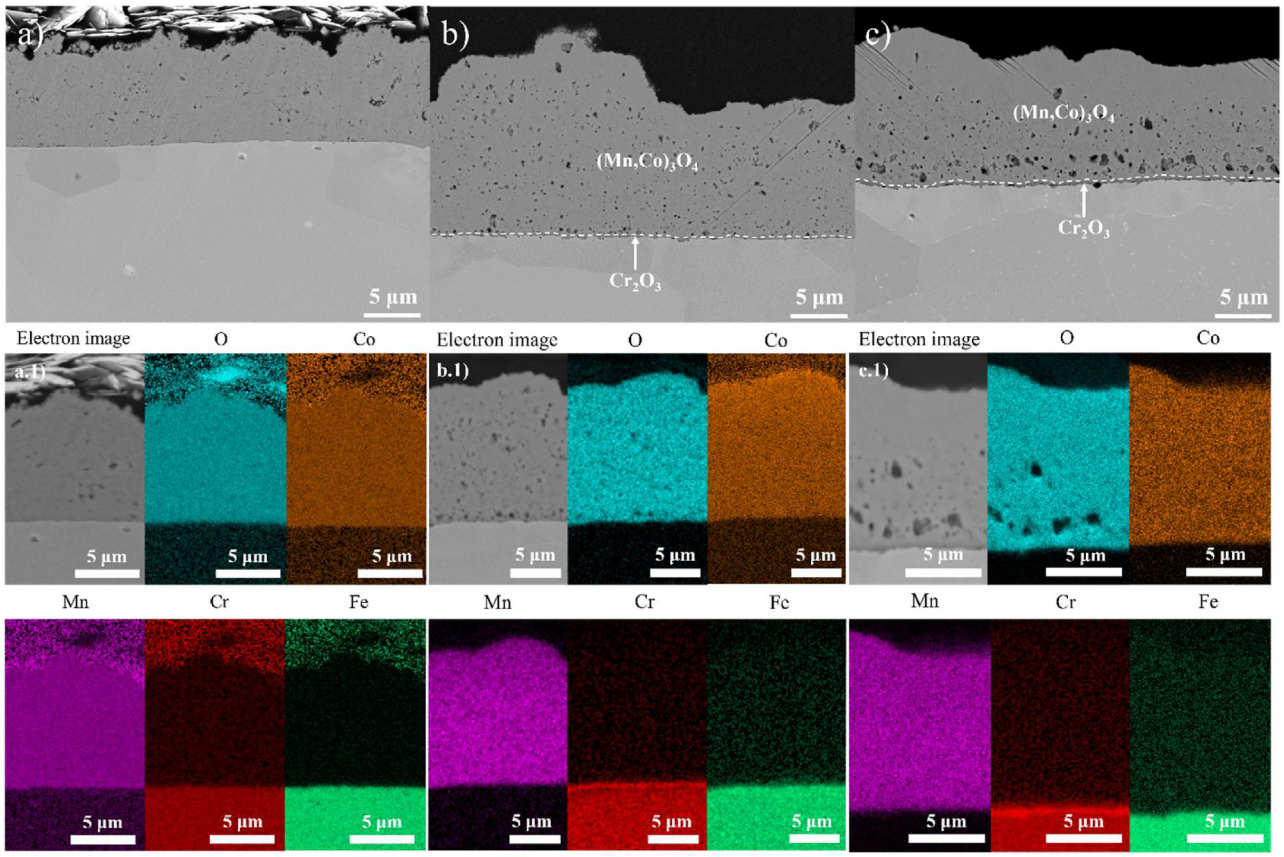

Fig. 6 – a) BIB-milled cross-section of the TS Mn/Co-coated sample in the absence of exposure. b) BIB-milled cross-section of the TS Mn/Co-coated sample exposed at 650 °C in humid air for 24 h. c) BIB-milled cross-section of the TS Mn/Co-coated sample exposed at 650 °C in humid air for 1000 h, together with the corresponding EDS analysis.

layer, a $(Fe,Cr)_3O_4$ layer, and finally, at the metal/oxide interface, a continuous Cr_2O_3 layer. The Fe-rich oxide layer seems to be relatively porous. Based on the fast oxidation process within the first 24 h it is concluded that the Mn/Cu layer impedes the formation of a protective Cr_2O_3 layer underneath the coating. This leads to the formation of the Fe-rich oxide layer and the inward growing $(FeCr)_3O_4$ layer. The presence of the Fe-rich oxide layer after 24 h of exposure could explain the high mass gain at the start of the exposure Nevertheless during prolonged exposure a Cr rich scale is formed at the metal/oxide interface (Fig. 8c). This leads to a very low mass gain after 24 h and a similar morphology between the 24 h and the 1000 h sample. The low level of Cr evaporation measured throughout the exposure is attributed to the thick layers present on top of the substrate, which reduces the Cr diffusion rate.

Area-specific resistance measurements

Fig. 9 shows the ASR measurements performed on coated samples exposed for 1000 h at 650 °C in air + 3% water vapour.

The PVD Ce/Co-coated samples exhibited an ASR of about 3 mΩ cm^2 after 1000 h of exposure at 650 °C. Previous research conducted on Sanergy HT Ce/Co-coated samples [38] showed that Ce/Co-coated samples displayed ASR values of around 8 mΩ cm^2 after 500 h of exposure at 650 °C in air + 3% water vapour. This difference is considered to be marginal. PVD Ce/Cu-coated samples showed an ASR of about 15 mΩ cm^2 after the 1000 h of exposure, while the Ce/MnCu coating exhibited an ASR of about 28 mΩ cm^2. Those results are in line with those of the microstructural analysis. The PVD Ce/Cu-coated samples formed a very thin Cr_2O_3 layer (of roughly 200 nm), while the Ce/MnCu-coated samples formed large oxide nodules with a slightly thicker chromia scale (approximately 300 nm) underneath. As reported previously [47], the ASR mainly reflects the thickness of the Cr_2O_3 layer. For the PVD Ce/Cu coating, the presence of an intermediate spinel layer does not seem to significantly affect the conductivity of the interconnect, probably due to the higher conductivity of this layer compared to Cr_2O_3. Earlier studies [29] have shown that manganite spinels, such as $MnCo_2O_4$ (60 S cm^{-1} at 800 °C) or $Cu_{1.3}Mn_{1.7}O_4$ (225 S cm^{-1} at 750 °C) are the most conductive spinels, and a CuO oxide layer is known to be conductive at high temperature (2×10^3 S cm^{-1} at 700 °C; 10^5 S cm^{-1} at 1000 °C) [48–50]. Thus, these oxides are three orders of magnitude more conductive than chromia, which have conductivities in the range of 0.001–0.05 S cm^{-1}, and thus do not significantly contribute to the overall resistance [51–53]. The pores that are observed in the oxidised coating are expected not to have a significant effect on ASR. Although, the pores reduce the effective cross-sectional area of the sample the pores are mainly present in the outer layer, which is expected to be highly conductive. PVD Ce/MnCu-coated samples exhibit

Please cite this article as: Tomas M et al., Efficiencies of cobalt- and copper-based coatings applied by different deposition processes for applications in intermediate-temperature solid oxide fuel cells, International Journal of Hydrogen Energy, https://doi.org/10.1016/j.ijhydene.2022.07.168

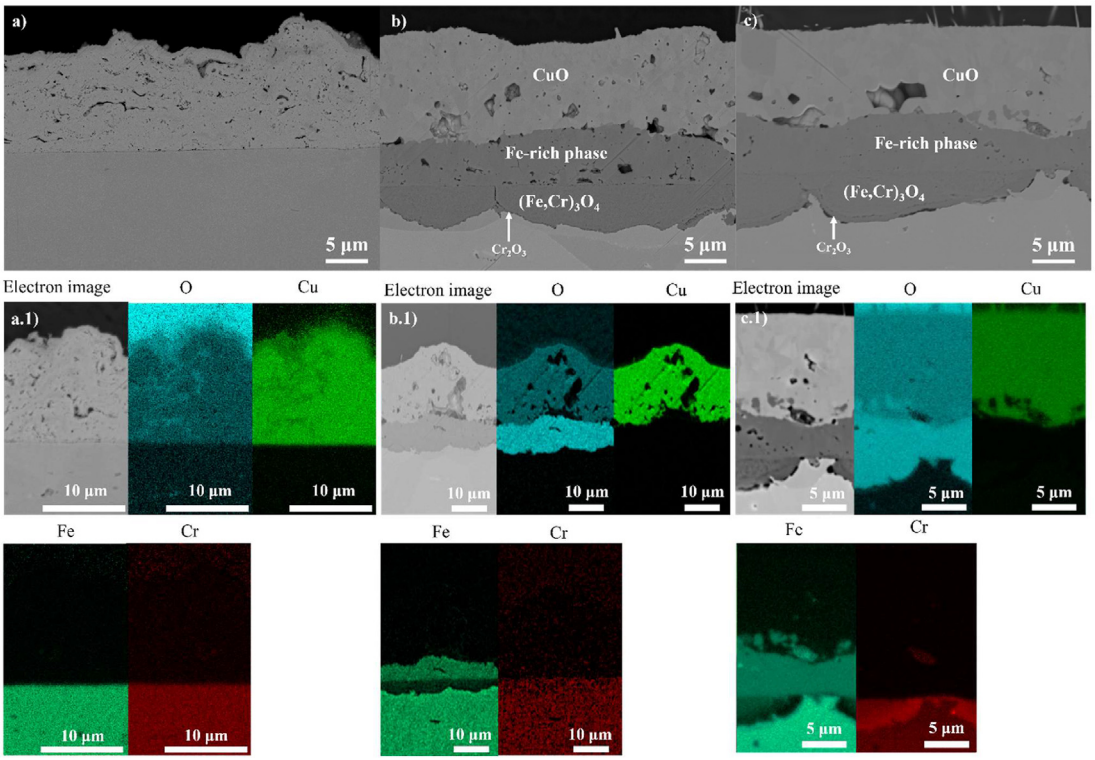

Fig. 7 – a) BIB-milled cross-section of the TS Cu-coated sample without exposure. b) BIB-milled cross-section of the TS Cu-coated sample exposed at 650 °C in humid air for 24 h. c) BIB-milled cross-section of TS Cu-coated sample exposed at 650 °C in humid air for 1000 h with the corresponding EDS analysis.

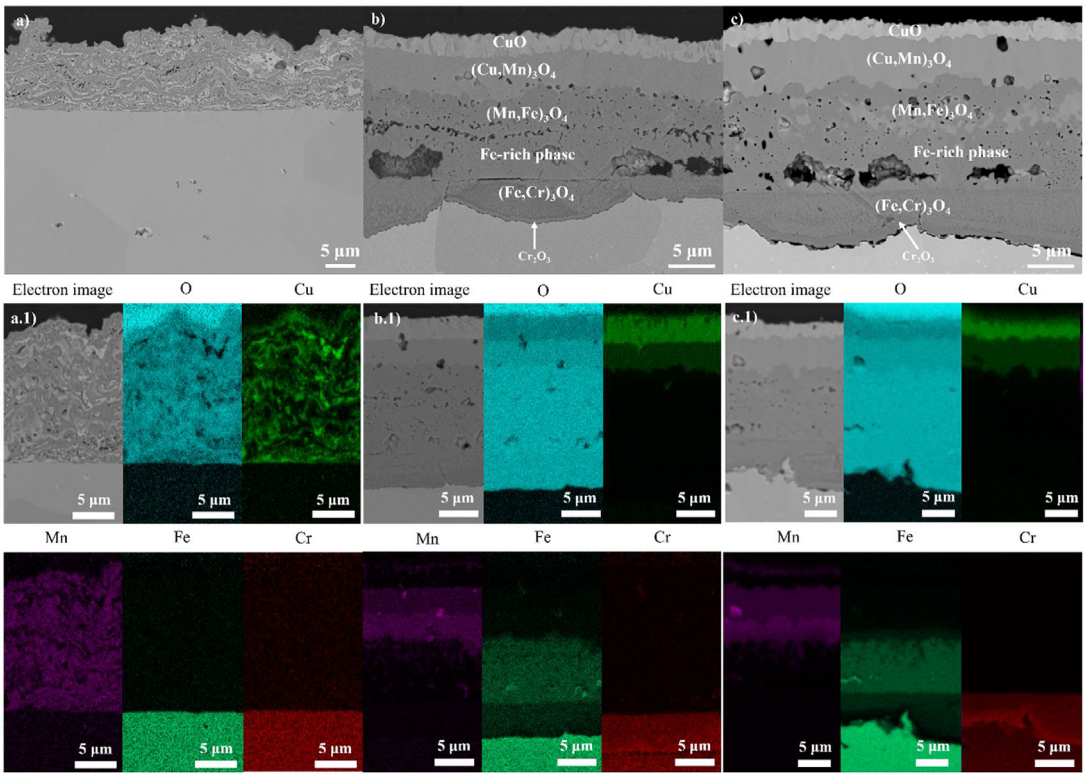

Fig. 8 – a) BIB-milled cross-section of TS Mn/Cu-coated sample without exposure. b) BIB-milled cross-section of the TS Mn/Cu-coated sample exposed at 650 °C in humid air for 24 h. c) BIB-milled cross-section of the TS Mn/Cu-coated sample exposed at 650 °C in humid air for 1000 h with the corresponding EDS analysis.

Please cite this article as: Tomas M et al., Efficiencies of cobalt- and copper-based coatings applied by different deposition processes for applications in intermediate-temperature solid oxide fuel cells, International Journal of Hydrogen Energy, https://doi.org/10.1016/j.ijhydene.2022.07.168

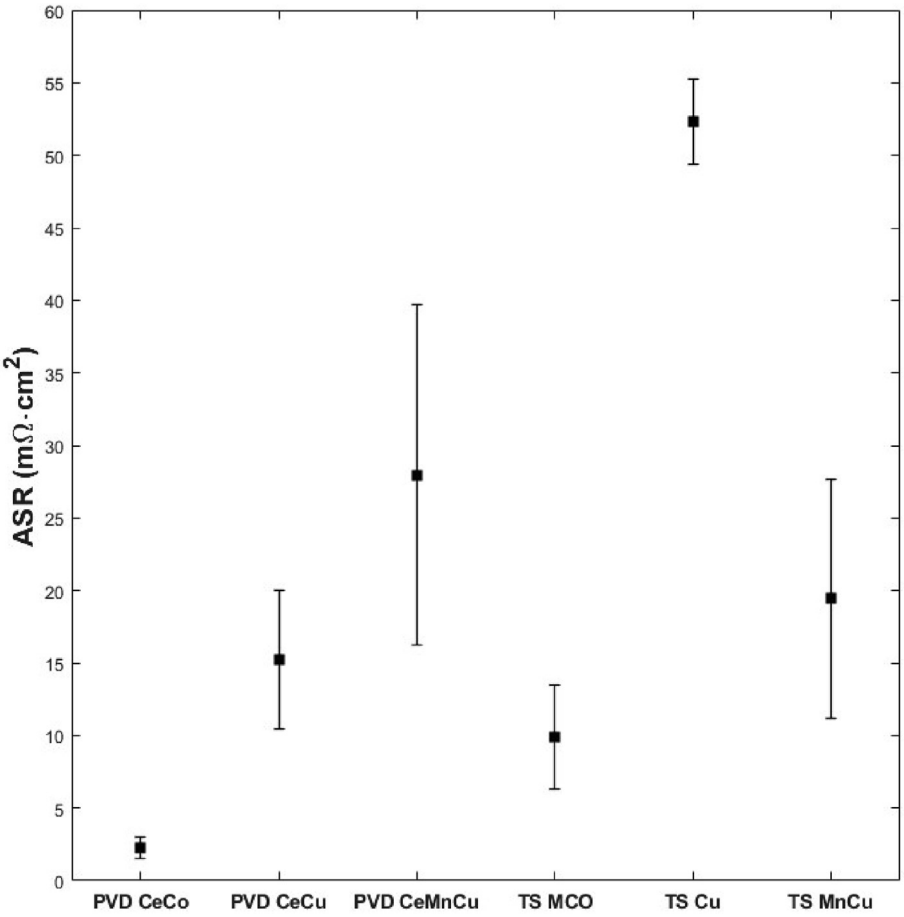

Fig. 9 – ASR measurements in air for samples exposed at 650 °C for 1000 h in air + 3% H_2O. Error bars indicate standard deviation.

somewhat higher ASR values, as a significant part of the surface (>50%) is covered with Fe-rich nodules. The conductivity of CeO_2 layer is expected to be quite low [54], however, due to the fact that it is very thin, and possibly discontinuous, the direct effect on ASR seems minimal. Additionally, the beneficial effect of Ce on maintaining a protective oxide scale seems to greatly outweigh the poor conductivity.

The TS Mn/Co coating exhibited a low ASR value, comparable to that of the PVD Ce/Cu coating. This accords with the observation of a thin Cr_2O_3 layer underneath the coating. In contrast, the TS Cu coating had the highest ASR value, which is attributed to a thicker Cr_2O_3 scale and the presence of an Fe-rich intermediate oxide scale (pure within the accuracy of EDS). The TS Mn/Cu coating exhibited these features as well but had a substantially lower ASR of 19 mΩ cm^2 on average. This might be due to the presence of Mn in the Fe-rich layer.

Overall, the PVD Ce/Co coating exhibits a lower ASR than the TS Mn/Co coating. However, since both samples exhibit very low ASR values, it is not clear whether this difference is significant.

Summary

The present study has focused on Cu-based coatings on AISI 441 steel. The coatings were manufactured using two different deposition methods: PVD and TS. The PVD coatings were deposited as a metallic coating and oxidised during the first stage of the exposure. The TS coatings consisted of a mostly oxidised coating sprayed on top of the substrate. In this study, uncoated, PVD Ce/Cu-, PVD Ce/MnCu-, PVD Ce/Co (as a reference for PVD coatings), TS Cu-, TS Mn/Cu- and TS Mn/Co- (as reference for TS coatings) coated samples were analysed.

Uncoated samples have the highest level of Cr(VI) evaporation. The observed difference between the PVD and TS coatings can be attributed to the uncoated edges of the PVD-coated samples. It is concluded that PVD coated samples seem to be as effective as TS coated samples at reducing Cr(VI) evaporation despite the much thinner (roughly 10 times thinner) coating.

The PVD Ce/Co- and Ce/Cu-coated samples, as well as the TS Mn/Co-coated sample, have ASR values < 15 mΩ cm^2. The PVD Ce/MnCu-coated samples display a somewhat higher ASR after 1000 h of exposure. This is attributed to the nodules on top of the scale. The TS Mn/Cu-coated sample has a similar ASR to the PVD Ce/MnCu-coated sample, while TS Cu coating gives the highest ASR values. PVD Ce/Cu coating is a good candidate to replace the state-of-the-art PVD Ce/Co coating. It offers a low level of Cr(VI) evaporation and thin, adherent, and conductive oxide scales. At intermediate temperatures, PVD Ce/Cu-coated samples form a conductive

Please cite this article as: Tomas M et al., Efficiencies of cobalt- and copper-based coatings applied by different deposition processes for applications in intermediate-temperature solid oxide fuel cells, International Journal of Hydrogen Energy, https://doi.org/10.1016/j.ijhydene.2022.07.168

CuO top layer, a conductive $(Cu,Cr,Mn,Fe)_3O_4$ intermediate spinel, and a very thin Cr_2O_3 layer at the metal/oxide interface. The formation of oxide nodules does not seem to influence the overall conductivity or the corrosion properties of the coated steel.

Declaration of competing interest

The authors declare the following financial interests/personal relationships which may be considered as potential competing interests: The author Jouni Puranen is employed at Elcogen OY and provided the thermal spray coated samples, realised by Kuopion Konepaja Oy. All experiments and characterization were carried out at Chalmers.

Acknowledgements

This work was conducted at the Swedish High Temperature Corrosion Centre (HTC) at Chalmers University of Technology. This work was performed in part at the Chalmers Material Analysis Laboratory, CMAL. The authors are grateful for funding by the Swedish Energy Agency through grant 2015-009652 and the Fordonsstrategisk forskning och innovation (FFI) program.

REFERENCES

[1] Beretta GP. World energy consumption and resources: an outlook for the rest of the century. Int J Environ Technol Manag 2007;7(1–2):99–112.
[2] Carrette L, Friedrich KA, Stimming UJC. Fuel cells: principles, types, fuels, and applications. ChemPhysChem 2000;1(4):162–93.
[3] Bvumbe TJ, et al. Review on management, mechanisms and modelling of thermal processes in PEMFC. Hydrogen Fuel Cells 2016;1(1):1–20.
[4] Powell M, et al. Demonstration of a highly efficient solid oxide fuel cell power system using adiabatic steam reforming and anode gas recirculation. J Power Sources 2012;205:377–84.
[5] Brandon N. Solid oxide fuel cell lifetime and reliability: critical challenges in fuel cells. Academic Press; 2017.
[6] Staffell I, Ingram A, Kendall K. Energy and carbon payback times for solid oxide fuel cell based domestic CHP. Int J Hydrogen Energy 2012;37(3):2509–23.
[7] Stambouli AB, Traversa E. Solid oxide fuel cells (SOFCs): a review of an environmentally clean and efficient source of energy. Renew Sustain Energy Rev 2002;6(5):433–55.
[8] Mah JC, et al. Metallic interconnects for solid oxide fuel cell: a review on protective coating and deposition techniques. Int J Hydrogen Energy 2017;42(14):9219–29.
[9] Jeffrey W, Fergus RH, Li Xianguo, Wilkinson David P, Zhang Jiujun. Solid oxide fuel cells: materials properties and performance. Taylor & Francis Group LLC; 2009.
[10] Mahato N, et al. Progress in material selection for solid oxide fuel cell technology: a review. Prog Mater Sci 2015;72:141–337.
[11] Hilpert K, et al. Chromium vapor species over solid oxide fuel cell interconnect materials and their potential for degradation processes. J Electrochem Soc 1996;143(11):3642–7.
[12] Stanislowski M, et al. Chromium vaporization from high-temperature alloys I. Chromia-forming steels and the influence of outer oxide layers. J Electrochem Soc 2007;vol. 154(4):A295–306.
[13] Molin S, et al. Low temperature processed MnCo2O4 and MnCo1.8Fe0.2O4 as effective protective coatings for solid oxide fuel cell interconnects at 750 C. J Power Sources 2016;336:408–18.
[14] Zanchi E, et al. Electrophoretic co-deposition of Mn1.5Co1.5O4, Fe2O3 and CuO: unravelling the effect of simultaneous addition of Cu and Fe on the microstructural, thermo-mechanical and corrosion properties of in-situ modified spinel coatings for solid oxide cell interconnects. J Eur Ceram Soc 2022;42(7):3271–81.
[15] Puranen J, et al. Characterization of high-velocity solution precursor flame-sprayed manganese cobalt oxide spinel coatings for metallic SOFC interconnectors. J Therm Spray Technol 2013;22(5):622–30.
[16] Shaigan N, et al. A review of recent progress in coatings, surface modifications and alloy developments for solid oxide fuel cell ferritic stainless steel interconnects. J Power Sources 2010;195(6):1529–42.
[17] Kurokawa H, et al. Chromium vaporization of bare and of coated iron–chromium alloys at 1073 K. Solid State Ionics 2007;178(3–4):287–96.
[18] Trebbels R, Markus T, Singheiser L. Investigation of chromium vaporization from interconnector steels with spinel coatings. J Fuel Cell Sci Technol 2010;7(1).
[19] Fontana S, Chevalier S, Caboche G. Metallic interconnects for solid oxide fuel cell: performance of reactive element oxide coating during 10, 20 and 30 months exposure. Oxid Metals 2012;78(5):307–28.
[20] Hou P, Stringer J. The effect of reactive element additions on the selective oxidation, growth and adhesion of chromia scales. Mater Sci Eng, A 1995;202(1–2):1–10.
[21] Hou PY. The reactive element effect–past, present and future. In: Materials science forum. Trans Tech Publ; 2011.
[22] Naumenko D, Pint B, Quadakkers WJOOM. Current thoughts on reactive element effects in alumina-forming systems: In memory of John Stringer. Oxid Met 2016;86(1–2):1–43.
[23] Stringer J. The reactive element effect in high-temperature corrosion. Mater Sci Eng, A 1989;120:129–37.
[24] Holmberg H, M WL, Westlinder J. Recent development in pre-coating of stainless steel strips for interconnects at Sandvik materials technology. In: 10th European SOFC forum; 2012.
[25] Grolig JG, et al. Copper based conversion coatings on ferritic stainless strip steel as solid oxide fuel cell interconnects: oxidation performance and chromium evaporation. ECS Trans 2013;57(1):2339–47.
[26] Waluyo NS, et al. Protective coating based on manganese–copper oxide for solid oxide fuel cell interconnects: plasma spray coating and performance evaluation. Ceram Int 2018;44(10):11576–81.
[27] Tomas M, et al. Cu-based coatings for IT-SOFC applications. ECS Trans 2019;91(1):2291.
[28] Lv Y, Geng S, Shi Z. Evaluation of electroplated copper coating on ferritic stainless steel for solid oxide fuel cells interconnects. J Alloys Compd 2017;726:269–75.
[29] Petric A, Ling H. Electrical conductivity and thermal expansion of spinels at elevated temperatures. J Am Ceram Soc 2007;90(5):1515–20.
[30] Directorate-General for Internal Market, I.. Entrepreneurship and SMEs and E. Commission. 2020. https://ec.europa.eu/growth/sectors/raw-materials/areas-specific-interest/critical-raw-materials_en.

Please cite this article as: Tomas M et al., Efficiencies of cobalt- and copper-based coatings applied by different deposition processes for applications in intermediate-temperature solid oxide fuel cells, International Journal of Hydrogen Energy, https://doi.org/10.1016/j.ijhydene.2022.07.168

[31] Prause L. Conflicts related to resources: the case of cobalt mining in the Democratic Republic of Congo. In: The material basis of energy transitions. Elsevier; 2020. p. 153–67.
[32] Farjana SH, Huda N, Mahmud MP. Life cycle assessment of cobalt extraction process. Journal of Sustainable Mining 2019;18(3):150–61.
[33] Lundberg MW, et al. Novel multilayered PVD-coating in a roll to roll mass production process. ECS Trans 2013;57(1):2203.
[34] Pawlowski L. The science and engineering of thermal spray coatings. John Wiley & Sons; 2008.
[35] Sidhu T, Prakash S, Agrawal R. State of the art of HVOF coating investigations-a review. Mar Technol Soc J 2005;39(2).
[36] Froitzheim J, et al. Investigation of chromium volatilization from FeCr interconnects by a denuder technique. J Electrochem Soc 2010;157(9):B1295–300.
[37] Tedmon Jr C. The effect of oxide volatilization on the oxidation kinetics of Cr and Fe-Cr alloys. J Electrochem Soc 1966;113(8):766.
[38] Falk-Windisch H, et al. Co- and Ce/Co-coated ferritic stainless steel as interconnect material for intermediate temperature solid oxide fuel cells. J Power Sources 2017;343:1–10.
[39] Falk-Windisch H, Svensson JE, Froitzheim J. The effect of temperature on chromium vaporization and oxide scale growth on interconnect steels for solid oxide fuel cells. J Power Sources 2015;287:25–35.
[40] Reddy MJ, Svensson J-E, Froitzheim J. Reevaluating the Cr evaporation characteristics of Ce/Co coatings for interconnect applications. ECS Trans 2021;103(1):1899.
[41] Talic B, et al. Effect of coating density on oxidation resistance and Cr vaporization from solid oxide fuel cell interconnects. J Power Sources 2017;354:57–67.
[42] Gunduz KO, et al. The effect of hydrogen on the breakdown of the protective oxide scale in solid oxide fuel cell interconnects. Corrosion Sci 2021;179:109112.
[43] Evans H, Donaldson A, Gilmour T. Mechanisms of breakaway oxidation and application to a chromia-forming steel. Oxid Metals 1999;52(5):379–402.
[44] Lumpp JK, Chen N, Goretta KC. Mechanical properties of CuO. High Temp Mater Process 1990;9(1):1–6.
[45] Talic B, et al. Diffusion couple study of the interaction between Cr2O3 and MnCo2O4 doped with Fe and Cu. Solid State Ionics 2019;332:16–24.
[46] Whittle D, Stringer J. Improvements in high temperature oxidation resistance by additions of reactive elements or oxide dispersions. Phil Trans Roy Soc Lond Math Phys Sci 1980;295(1413):309–29.
[47] Goebel C, et al. Does the conductivity of interconnect coatings matter for solid oxide fuel cell applications? J Power Sources 2018;383:110–4.
[48] Meyer B, et al. Binary copper oxide semiconductors: from materials towards devices. Phys Status Solidi 2012;249(8):1487–509.
[49] Zoolfakar AS, et al. Nanostructured copper oxide semiconductors: a perspective on materials, synthesis methods and applications. J Mater Chem C 2014;2(27):5247–70.
[50] Samsonov GV. The oxide handbook. Springer Science & Business Media; 2013.
[51] Huczkowski P, et al. Growth mechanisms and electrical conductivity of oxide scales on ferritic steels proposed as interconnect materials for SOFC's. Fuel Cell 2006;6(2):93–9.
[52] Crawford JA, Vest RW. Electrical conductivity of single-crystal Cr2O3. J Appl Phys 1964;35(8):2413–8.
[53] Holt A, Kofstad P. Electrical conductivity and defect structure of Cr2O3. I. High temperatures (>~ 1000° C). Solid State Ionics 1994;69(2):127–36.
[54] Suzuki T, Kosacki I, Anderson HU. Microstructure–electrical conductivity relationships in nanocrystalline ceria thin films. Solid State Ionics 2002;151(1–4):111–21.

Please cite this article as: Tomas M et al., Efficiencies of cobalt- and copper-based coatings applied by different deposition processes for applications in intermediate-temperature solid oxide fuel cells, International Journal of Hydrogen Energy, https://doi.org/10.1016/j.ijhydene.2022.07.168